Quantum Dot Photovoltaics in the Extreme Quantum Confinement Regime: The Surface-Chemical Origins of Exceptional Air- and Light-Stability

Jiang Tang,[†,‡] Lukasz Brzozowski,[‡] D. Aaron R. Barkhouse,[‡] Xihua Wang,[‡] Ratan Debnath,[‡] Remigiusz Wolowiec,[‡] Elenita Palmiano,[‡] Larissa Levina,[‡] Andras G. Pattantyus-Abraham,[‡] Damir Jamakosmanovic,[‡] and Edward H. Sargent[†,‡,*]

[†]Department of Materials Science and Engineering, University of Toronto, 184 College Street, Toronto, Ontario M5S 3E4, Canada, and [‡]Department of Electrical and Computer Engineering, University of Toronto, 10 King's College Road, Toronto, Ontario M5S 3G4, Canada

ABSTRACT We report colloidal quantum dot (CQDs) photovoltaics having a ~930 nm bandgap. The devices exhibit AM1.5G power conversion efficiencies in excess of 2%. Remarkably, the devices are stable in air under many tens of hours of solar illumination without the need for encapsulation. We explore herein the origins of this orders-of-magnitude improvement in air stability compared to larger PbS dots. We find that small and large dots form dramatically different oxidation products, with small dots forming lead sulfite primarily and large dots, lead sulfate. The lead sulfite produced on small dots results in shallow electron traps that are compatible with excellent device performance; whereas the sulfates formed on large dots lead to deep traps, midgap recombination, and consequent catastrophic loss of performance. We propose and offer evidence in support of an explanation based on the high rate of oxidation of sulfur-rich surfaces preponderant in highly faceted large-diameter PbS colloidal quantum dots.

KEYWORDS: colloidal quantum dot photovoltaics · surface spectroscopy · oxidation products · optoelectronic device stability · traps · recombination · and transport in colloidal quantum dot solids

Photovoltaics based on solution-processing offer an avenue to low-cost harvesting of the sun's abundant power reaching the earth. One opportunity for further improvement in solution-cast solar cells' efficiency lies in making better use of the sun's full spectrum, including the infrared portion. Polymer solar cells typically absorb out to 650 or 700 nm,[1] whereas the optimum bandgap of a single-junction solar cell lies in the vicinity of 1000 nm.

Colloidal quantum dot (CQD) photovoltaics offer the benefits of solution-processing combined with the potential to harvest the sun's visible, near-infrared, and short-wavelength infrared rays.[2] CQD solar cells have seen rapid advances in recent years, progressing from the first report of an infrared CQD solar cell[3] to recent reports of 1.8% AM1.5 power conversion efficiency (PCE) using PbS,[4] 2.1% AM1.5 PCE using PbSe,[5] and 3.4% AM1.5 PCE using PbS_xSe_{1-x}.[6]

These recent reports have focused on lead chalcogenide nanocrystals (NCs) with diameters in the range 4−10 nm, and, correspondingly, excitonic peaks between 1.2 and 1.8 μm wavelength. Such devices are of interest in the investigation of possible harvesting of multiple excitons,[7−9] and also as the small-bandgap junction in a tandem or triple-junction cell.

However, the potential to realize an optimal-bandgap single-junction solar cell employing CQDs motivates investigations of photovoltaic devices having a ~950 to 1000 nm quantum-confined bandgap. Realizing such devices using PbS would entail the use of quantum dots having ~3 nm diameter—vastly smaller than the ~20 nm Bohr exciton radius in PbS. One may also present the extremes of this regime in energy: whereas the bulk bandgap of PbS is 0.4 eV, the quantum-confined bandgap of the optimal-bandgap CQD solar cell is closer to 1.3 eV. Thus, in such devices, the considerable majority of bandgap energy comes from quantum confinement.

A number of questions arise in this regime of extreme quantum confinement:

(1) Can colloidal quantum dot synthesis be made sufficiently monodisperse and reproducible within this spectral regime? Does the heightened sensitivity, within the extreme confinement regime, to the size distribution within the resultant population of NCs result in broad excitonic structure and a loss in sharpness in absorption onset?

*Address correspondence to ted.sargent@utoronto.ca.

Received for review November 5, 2009 and accepted January 15, 2010.

Published online January 27, 2010. 10.1021/nn901564q

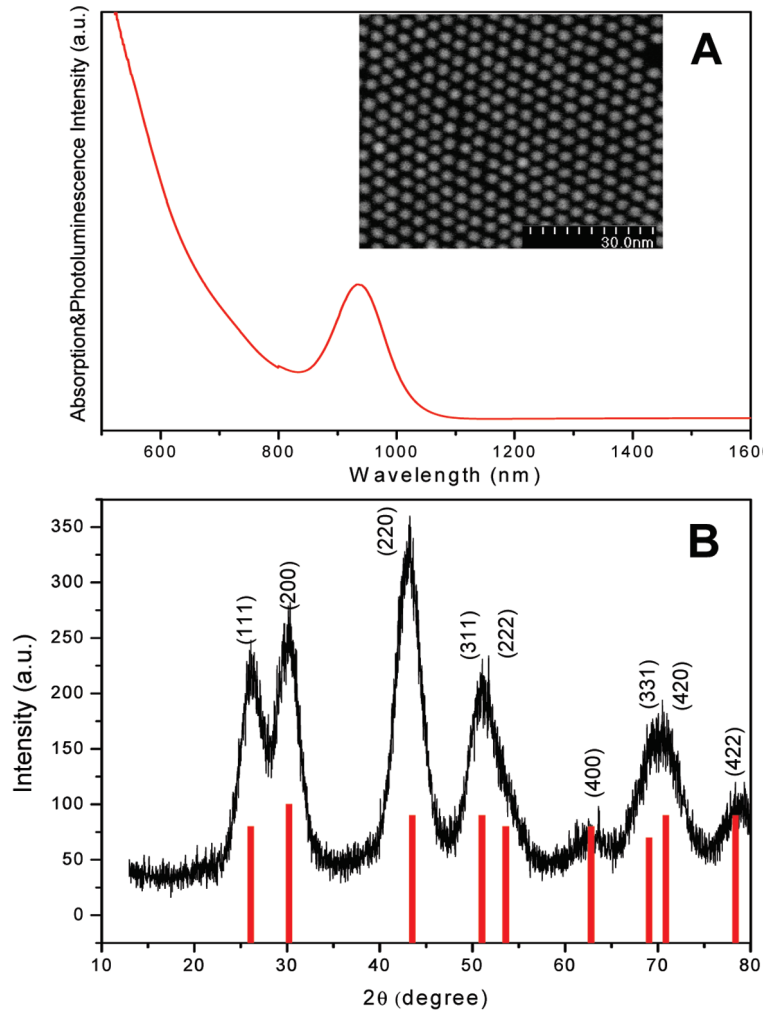

Figure 1. (A) Absorption spectrum of as-synthesized PbS NCs in toluene. Inset is an STEM image of PbS NCs showing local hexagonal ordering. (B) XRD of PbS colloidal quantum dot films. The standard diffraction pattern (JCPDS 02-0699) for bulk PbS is included as inset in Figure 1B.

(2) Might new trap states (either shallow traps for one carrier type, or midgap traps that serve as recombination centers for electron−hole pairs) emerge in these highly confined systems that (i) prevent the formation of high built-in-potential Schottky barriers that enable efficient carrier separation; (ii) dramatically alter the free-carrier density, producing either depletion regions that are too narrow (hence insufficiently optically absorptive) or too wide (hence too low in charge-separating field) to produce high quantum efficiencies; (iii) increase nonradiative recombination to the point of reduced internal quantum efficiency.

To answer these questions, we report herein the realization and characterization of CQD solar cells based on lead chalcogenide quantum dots whose first excitonic peak lies near the optimal single-junction bandgap. Specifically, we employ PbS NCs synthesized in oleic acid and having a 930 nm excitonic peak.

RESULTS

Synthesis and Characterization PbS NCs. We carried out synthesis using lead oleate and bis(trimethylsilyl) sulfide (TMS) as precursors.[10] We use a Pb to S precursor ratio set as 2:1, within the typical range employed in cadmium chalcogenide and lead chalcogenide NC synthesis.[11] We employed slow cooling following sulfur precursor injection to facilitate size focusing in the hope of achieving a narrow size distribution and well-defined excitonic structure.

As seen in Figure 1A, as-synthesized PbS NCs showed a well-defined excitonic peak centered at 930 nm. The full width at half-maximum (fwhm) of the absorption peak was ~100 nm. We imaged the NCs using scanning transmission electron microscopy (STEM) as seen in the inset of Figure 1A. The average size of the PbS NCs was ~3 nm, in perfect agreement with the number calculated from eq 1 proposed by Iwan Moreels *et al.*[12]

$$E_0 = 0.41 + (0.0252d^2 + 0.283d)^{-1}$$

where E_0, the bandgap in unit of eV, is 1.33 eV in our case. The ordered hexagonal packing is consistent with a narrow distribution in NC diameter.

From a simple model[13] of the dependence of quantum-confined bandgap on NC diameter, we estimate that the standard deviation in NC diameter was less than 10%. For the 3 nm NCs discussed herein, this variation in diameter lies well below the lattice constant of the constituent PbS crystal, indicating better-than-monolayer monodispersity.

We employed powder X-ray diffraction (XRD) to investigate the phase, crystal size, and crystallinity of the NCs. For six batches of nominally identically synthesized NCs, the position of diffraction peaks agreed with the standard diffraction patterns of face-centered cubic PbS (JCPDS 02-0699, $a = 0.593000$ nm), as seen in Figure 1B. We were unable to detect any impurity phases in any sample. We determined the lattice constant, the mean domain size (equivalent to the nanocrystal size in our case), and the crystallinity percentage, all using Rietveld refinement of XRD data (Supporting Information, Figure S1) using Topas V2.1 profile fitting software.[14] We summarize the results in Supporting Information, Table S1.

We determined the lattice constant to be 0.5969 ± 0.0004 nm which, interestingly, is greater within experimental uncertainty than the 0.593 nm standard. This finding is consistent with past observation in CdTe NCs[15] and has been attributed to the effects of surface tension in small crystals. The mean domain size was found to be 2.8 ± 0.2 nm, consistent with TEM measurements of NC size. We conclude that our NCs are single-crystalline.

We sought to elucidate further the average composition of the NCs using inductively coupled plasma atomic emission spectroscopy (AES-ICP). We rinsed our samples thoroughly with methanol for five times to remove any lead oleate residue from the synthesis. All samples measured were found to be Pb-rich: the average Pb to S ratio was 1.8 ± 0.1. Similar findings have been reported for PbS[12] and PbSe NCs,[16] and we offer a similar explanation: taking XRD and ICP results together, we propose that the NCs consist of a stoichiometric PbS 1:1 core crystal surrounded with a Pb^{2+}-terminated surface shell.[17]

Fabrication of PbS Quantum Dot Films. Prior to fabricating films, we isolated the NCs by precipitating using a nonsolvent. We then redispersed in oleylamine for a two-day exchange to a similarly long, but less strongly bound, ligand compared to the original oleic acid. This partial exchange was accompanied by a 10 nm blue-shift in absorption. We precipitated the dots with methanol and then redispersed the resultant materials at a concentration of 10 mg/mL in octane for device fabrication.

Layer-by-layer fabrication of CQD films has recently been reported in the fabrication of field-effect transistors[18] as well as photovoltaics.[5,6,19−21] In each case, a bidentate ligand such as hydrazine, ethanedithiol (EDT), and benzenedithiol has been explored. One primary goal of the new ligand is to displace long insulating original ligands, shrinking the internanocrystals spacing, and enabling improved electron and hole transport. The end functional group itself plays an important role[22] in the passivation of the NC surface and thus the control of midgap states and shallow traps.[23]

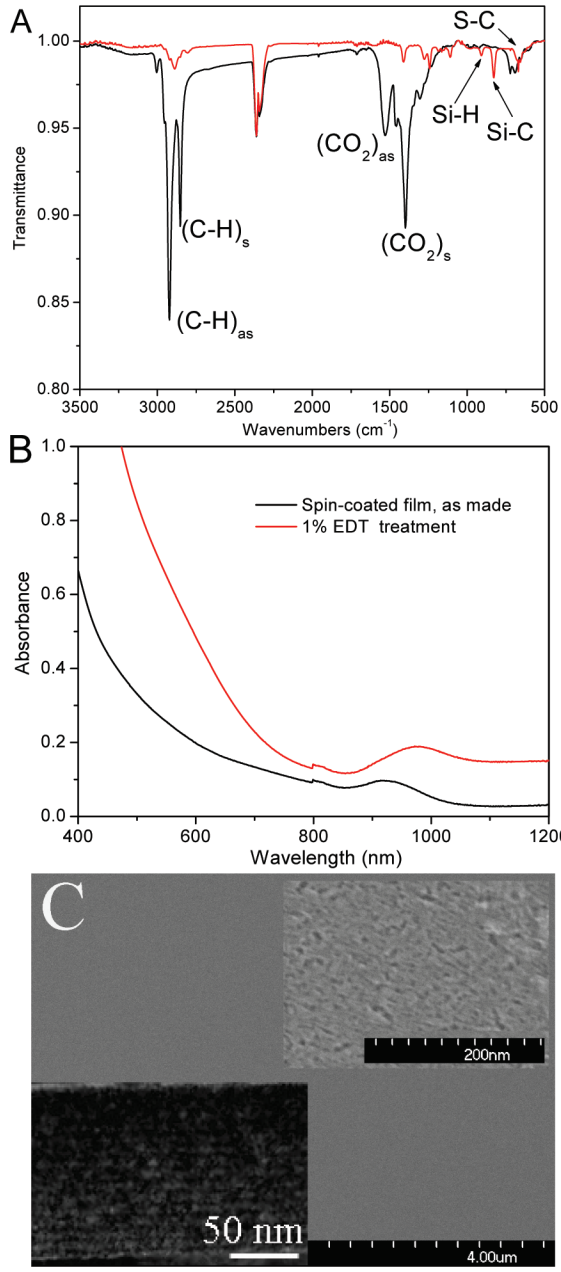

Figure 2. (A) FTIR spectra of spin-coated PbS NCs film (black) and after 1% EDT solution treatment. The strong CO_2 vibration peak at 2358 cm^{-1} is due to inequalities in beam path length. (B) Absorption spectra of as-spin-coated PbS film (black) and film treated using 1% EDT in acetonitrile (red). (C) SEM characterization of 15 LBL PbS film. High resolution top-view SEM image is included in top right and high resolution cross-section TEM image is included in bottom left.

We used layer-by-layer coating to build films and found that the original oleic acids were completely removed following the EDT treatment: as seen in Figure 2A, the strong symmetrical and asymmetrical —$(CO_2)^-$

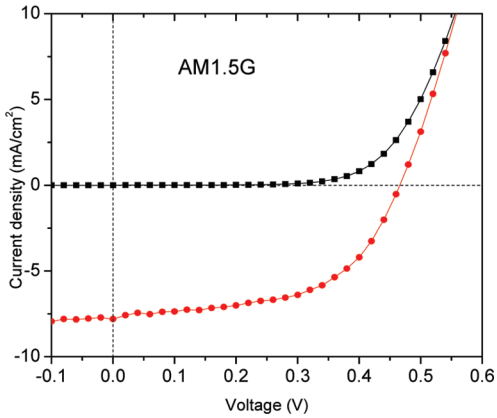

Figure 3. Current−voltage characteristics of the device under 100 mW/cm² AM1.5G irradiation.

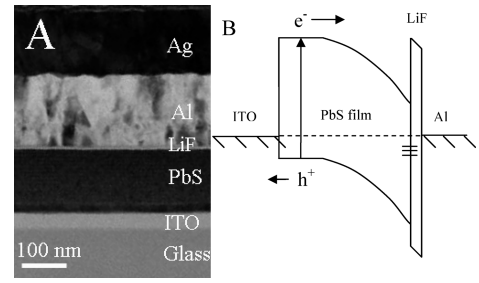

Figure 4. (A) Cross-section high-resolution TEM image of the Schottky device: Glass/ITO/PbS/LiF/Al/Ag. (B) Proposed equilibrium band diagram in the dark. The p-type PbS film is composed of quasi-neutral region (flat band) on the ITO side and depletion region (bended band) on the Al side. The dashed line represents the work function and the parallel short bars represent interfacial traps.

vibration at 1398 and 1528 cm^{-1}, characteristic of the carboxylate functional group in oleic acid, is absent. Commensurate with removal of oleic acid was the appearance of C−S stretch peaks at 655, 669, and 680 cm^{-1}, and CH_2 stretching peaks at 2849 and 2918 cm^{-1}, confirming the presence of EDT in the film.[24] The excitonic peak shifted from 914 nm in untreated films to 972 nm in EDT treated films (Figure 2B). This is consistent with enhanced internanocrystals electronic coupling that is one of the primary goals of the dithiol treatment process.[21] Fifteen layers of repeated layer-by-layer deposition produces films ~130 nm thick corresponding to a deposition rate of three quantum dot layers per cycle.

Device Performance and Stability. We systematically optimized the device fabrication procedure, and the key steps to achieve high efficiency are to treat the film when it spins, 90 °C air annealing, and introduction of LiF. The fabrication procedure that produced the highest-performance devices reported herein involved the deposition of 15 layers on an ITO-coated glass substrate, completed by the evaporative deposition of a top contact consisting of 0.8 nm LiF, 100 nm of Al, and 100 nm of Ag contact of 0.96 mm radius.

The current−voltage characteristics of our best representative device under 100 mW/cm² AM1.5G irradiation are shown in Figure 3. We employed an active area of 2.9 mm². The best device exhibited a short-circuit current (J_{sc}) density of 8.57 mA/cm², an open circuit voltage (V_{oc}) of 0.46 V, and a fill factor (FF) of 54.5%. These devices provided a maximum AM1.5G PCE of 2.15%. This is the highest AM1.5G power conversion efficiency reported using PbS colloidal quantum dots.

Recent reports of comparable and somewhat higher AM1.5 PCEs using PbSe and PbSSe required that all fabrication and characterization be carried out inside the inert environment provided by a N_2 or Ar glovebox.[5,6,25] In contrast, the devices reported herein were fabricated, characterized, and stored entirely in ambient environment. Following 63 h continuous and simultaneous 100 mW/cm² AM1.5G illumination and current−voltage scanning in air, the unencapsulated devices retained >87% of their initial power conversion efficiency.[26]

Device Operation Mechanisms. We show in Figure 4 the device structure (TEM, Figure 4A) and the proposed spatial band diagram (Figure 4B).

On the basis of a previous report using absorption spectra and cyclic voltammetry to determine the band alignment of various sized PbS NCs,[27] we estimate the quantum-confined conduction band of our PbS NCs lies at −3.8 eV and the valence band at −5.1 eV. In view of the p-type doping of air-exposed PbS, combined with the shallow work function Al (Φ = 4.2 eV), we expect a Schottky barrier to form at this metal−semiconductor junction, resulting in band bending and a depletion region. ITO (E_F = 4.8 eV) is expected to form an ohmic anode to the p-type PbS film. Under illumination, electron−hole pairs generated in the depletion region are separated by the built-in field, electrons traveling to the Al electrode and holes to the ITO.

We sought to learn more about carrier density and the depletion region in our devices. Capacitance−voltage studies, including the use of Mott−Schottky plots, provide a means to study this junction through the bias-dependence of its depletion capacitance. First, though, an estimate of the static relative permittivity ε of the quantum dot film was required. We employed carrier extraction *via* linearly increasing voltage (CELIV): a triangular voltage pulse, linearly increasing at a rate *A*, is applied to the device and the corresponding transient current is measured.[28,29] As shown in Figure 5A, we estimated the static relative permittivity ε from the displacement component j_0

$$\varepsilon = j_0 d / A\varepsilon_0 \quad (1)$$

where j_0 is displacement current density, *d* is device thickness, *A* is ramp rate, and ε_0 is the vacuum permittivity. We obtained ε of ~18, which is the typical value for PbS NCs film.

On the basis of the Maxwell−Garnett effective medium theory:

$$\varepsilon = \varepsilon_m \frac{\varepsilon_i(1 + 2\delta) - \varepsilon_m(2\delta - 2)}{\varepsilon_m(2 + \delta) + \varepsilon_i(1 - \delta)} \quad (2)$$

where ε, ε_m, ε_i are dielectric constant of the film, the matrix, and the embedded material, respectively, and δ is the volume fraction of the embedded material; we obtained an effective dielectric constant ε for the dot + matrix combination of approximately 20 using an ε_i of 169 for bulk PbS and ε_m of 5 for our ligands and assuming a volume fill fraction of inclusions (PbS quantum dots) of about 50%. The calculated value is in good agreement with our experimentally measured value.

Analysis of Mott−Schottky plots also requires knowledge of the built-in potential. We estimated this from $J-V$ data: by graphing net photocurrent (J_L-J_D), the difference between photocurrent and dark current, as a function of the voltage, we extracted the voltage at which the net photocurrent is equal to zero.[30] As seen in Figure 5B, the extracted V_{bi} is 0.52 V, consistent with the V_{oc} of 0.49 V in this device.

We proceeded to capacitance−voltage ($C-V$) characterization of our devices. The results are shown in Figure 5C. The 15-layer (~130 nm thickness) and 20-layer (~180 nm thick) devices show similar capacitance to one another in the reverse-biased region, whereas the capacitance for the 10-layer (~90 nm thickness) device is larger. This suggests that the 10-layer device is fully depleted while the 15-layer and thicker devices possess both a depletion region near the Al side and also a quasi-neutral region near the ITO.

The 10-layer device, if fully depleted, is predicted to have geometric capacitance equal to

$$C_0 = \varepsilon\varepsilon_0 A/W \quad (3)$$

where ε, ε_0, and A are the dielectric constant, vacuum permittivity, and device area, respectively. We measured the 10-layer device to have a capacitance of 5.9 nF. The predicted geometric capacitance, using ε =18 and the measured active layer thickness W = 90 nm, is 5.7 nF. The good agreement between these values is consistent with the view that this device is indeed fully depleted.

From the thicker devices, whose zero-bias capacitances were measured to 4.6 nF, we were able to estimate the depletion width to be approximately 110 nm. Given independent knowledge of V_{bi} we are able to estimate the acceptor density, N_A, in the depletion region from

$$N_A = 2\varepsilon\varepsilon_0 V_{bi}/(qW^2) \quad (4)$$

We determined from this an exposed acceptor density of 8×10^{16} cm^{-3}.

It is of interest to elucidate the implications of a fully depleted, compared to a mixed (quasi-neutral + depletion-region) device. Measurement of the spectrum of external quantum efficiency (EQE), and estimation from it and from the absorption spectrum of the internal quantum efficiency, allow an assessment of the fate of charge carriers generated in each region.

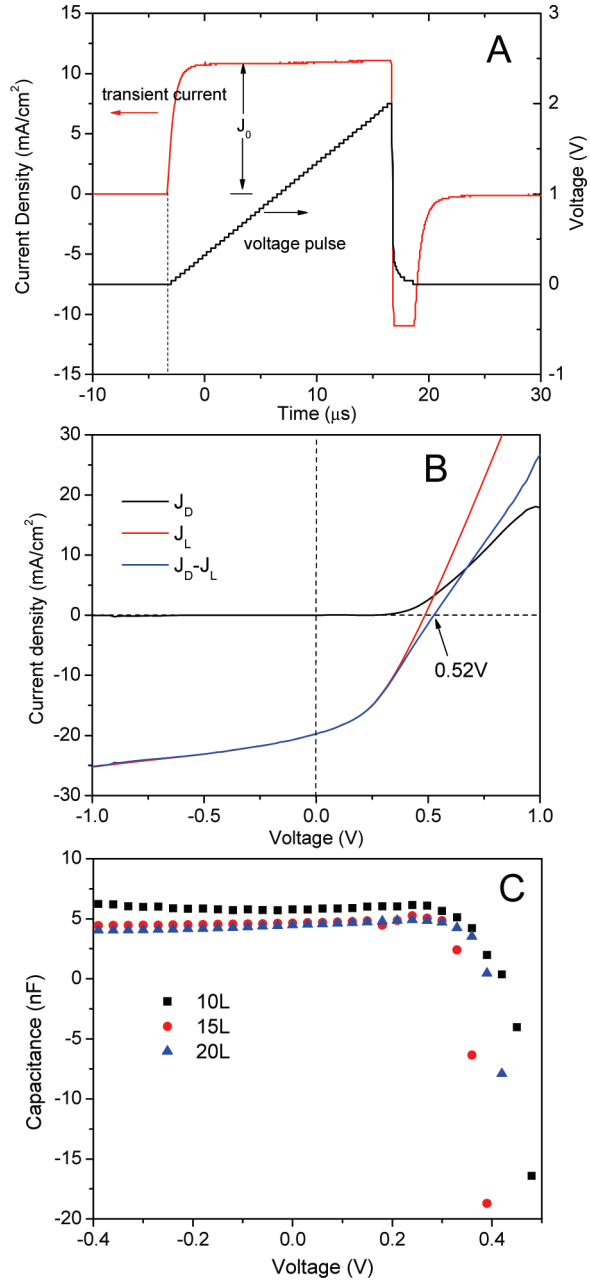

Figure 5. Determination of static relative permittivity, built-in potential, and depletion width of PbS NCs device. (A) CELIV, including the transient current density (red) produced as a result of application of the triangular voltage pulse (black). (B) $J-V$ characteristics of device in the dark and under irradiation. The photocurrent (J_L-J_D) is equal to zero at a compensation voltage of 0.52 V; (C) capacitance−voltage characterization of 10, 15, and 20 L devices.

We report in Figure 6 the absorption spectra and EQE spectra of the thin, medium, and thicker devices. In the case of the thin device, the spectral shapes of the EQE and absorbance spectra follow one another fairly closely. Since illumination is through the ITO, that is,

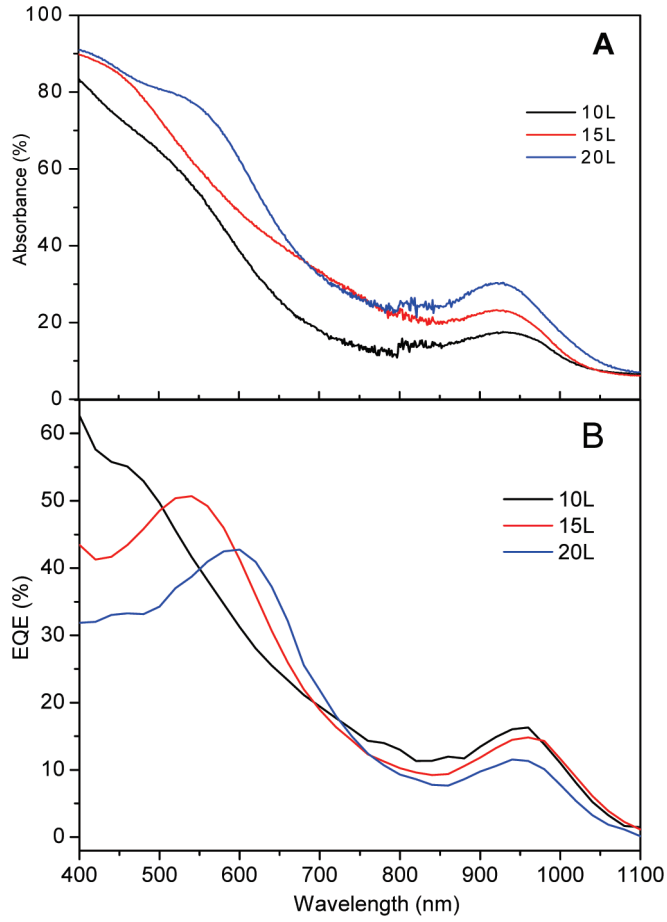

Figure 6. (A) Absorption spectra and (B) EQE spectra of 10, 15, and 20 L devices.

from the ohmic contact side instead of the Schottky contact side, we can conclude that electrons are capable of electrical-field-driven drift transport across the entire 90 nm distance prior to undergoing recombination. Since, from the transient response of the device (Supporting Information, Figure S3), we estimate the electron minority carrier lifetime to be in the tens of microseconds, we can conclude that the electron mobility must exceed 10^{-5} cm^2/(V s) to transit the device, with the aid of the built-in field, within the electrons' lifetime.

The EQE spectra of the non-fully depleted devices are dramatically different. Throughout the infrared and into the edge of the visible (the red), the absorbance and EQE spectra follow similar shapes. Charge carriers are generated reasonably uniformly throughout the thickness of the device at these wavelengths. However, once single-pass absorbance exceeds 50% as the wavelength is reduced into the visible and toward the blue region, carrier generation near the ohmic ITO contact—thus remote from the Schottky barrier—begins to dominate. At these short wavelengths, the EQE spectrum drops sharply. Given that absorbance is monotonically increasing going toward the blue in this spectral regime, it is clear that the short-wavelength IQE has diminished even more dramatically. We conclude that carriers generated in the quasi-neutral region are collected with much lower efficiency than those generated in the depletion region. From this, we can ascertain that the electron minority diffusion length is considerably less than the quasi-neutral region thickness. In the case of the 15-layer device, we estimate the quasi-neutral region thickness as (device thickness minus depletion region thickness) ≈ 20 nm. We conclude that the electron minority carrier diffusion length is very short indeed in these devices, a finding that is in stark contrast with the best PbS large-dot (defined as the PbS NCs with excitonic peak ~1500 nm) devices. A comparison of small and large PbS NCs devices characteristics are summarized in Table 1.

The Physical and Chemical Origins of Improved Device Lifetime and Robustness to Oxygen. Previous reports[4,5,25] on lead chalcogenide QCDs Schottky solar cells have described a lack of stability in air. The first high-efficiency reports employed butylamine-capped PbS nanoparticles, and the cells degraded in air within minutes;[5] the butylamine was suspected of reacting with the shallow-work-function metal contact. Passivating PbSe using 1,4-benzenedithiol led to devices stable in a glovebox over weeks, and in air over a few hours, a considerable improvement.[20] Other literature, reporting the use of ethanedithiol (EDT),[5,25] indicated that even removal of the devices for mere minutes from a glovebox produced rapid degradation.

The small-dot PbS Schottky solar cells reported herein showed much improved air stability: their pro-

TABLE 1. Characteristics Comparison of Small and Large PbS NCs Devices

	large dots	small dots
bandgap (eV)	0.8	1.3
crystallinity	100%	100%
averaged Pb:S ratio	1.5:1	1.8:1
oxidation products	mainly $PbSO_4$	mainly $PbSO_3$
relative permittivity ε	17	18
carrier density N_a	1×10^{17} cm^{-3}	8×10^{16} cm^{-3}
electron mobility μ_n	$\geq 1 \times 10^{-4}$ cm^2/(V s) by ToF	$>1 \times 10^{-5}$ cm^2/(V s) from IQE
diffusion length (L_n) in quasi-neutral region	~100 nm	<20 nm
carrier lifetime (τ_n)	~15 μs from V_{oc} decay	~16 μs from V_{oc} decay
IQE	>80%	>80%
air stability of devices	poor	good

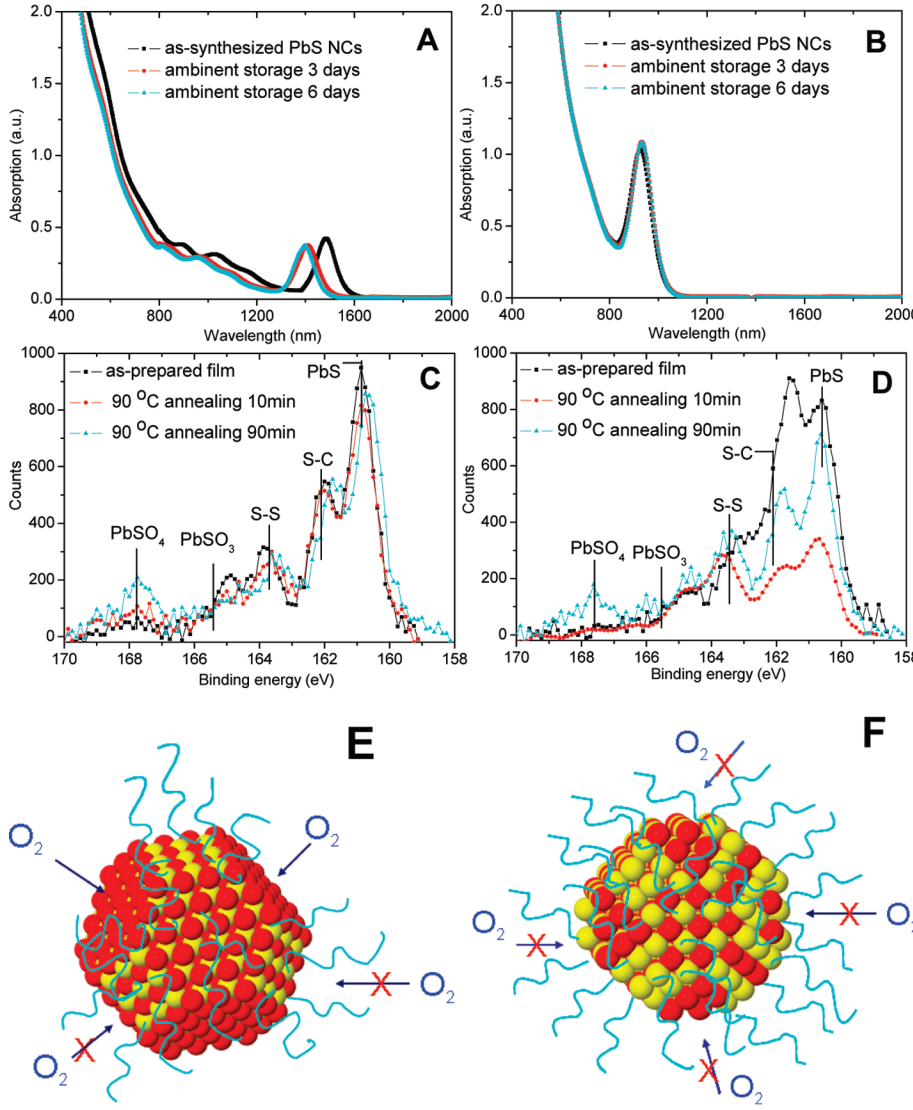

Figure 7. Comparison of oxidation characteristics of large (A, C, E) and small (B, D, F) PbS NCs. Absorption change of (A) large PbS NCs and (B) small PbS NCs stored in octane solution in ambient for 0 day (black), 3 days (red) and 6 days (cyan); XPS S 2p spectra of as-fabricated film (black), film annealed in air at 90 °C for 10 min (red) and annealed for 90 min (cyan) of large PbS NCs (C) and small PbS NCs (D). We use peaks at binding energy of 160.8 eV for PbS, 162.0 eV for S−C in ethanedithiol, 163.7 eV for S−S in oxidation products of ethanedithiol, 165.4 eV for $PbSO_3$, and 167.8 eV for $PbSO_4$.[31,32] Schematic illustration of oxidation for large (E) and small (F) PbS NCs. Large PbS NCs are faceted and small ones are spherical. The red spheres, yellow spheres, and cyan tails are dedicated to sulfur atoms, lead atoms in PbS NCs, and surface ligands, respectively.

cessing was performed in an air ambient, and, following 63 h continuous and simultaneous 100 mW/cm^2 AM1.5G illumination and current−voltage scanning in an air ambient, unencapsulated devices retained ~87% of their initial power conversion efficiency.[26]

We sought to investigate the origins of this remarkable enhancement. Our first study involved comparing the blue shift in the excitonic feature of small *versus* large dots. As shown in Figure 7A, as-synthesized large PbS NCs showed a 73 nm blue-shift in their excitonic peak in the first 3 days' ambient storage and another 15 nm in another 3 days' ambient storage. In striking contrast, small PbS NCs showed no blue-shift during ambient storage, as in Figure 7B. This overall 86 nm blue shift in large PbS NCs corresponds to a 0.5 nm reduction in PbS NCs diameter—the loss of a monolayer of PbS to oxidation.[17]

We then sought to compare the fate of the surface chemistry of small and large oxidized PbS dots using XPS. We fabricated PbS films using small and big PbS NCs following the same procedure employed herein in device fabrication. To accelerate the aging process, we annealed each sample at 90 °C in air for 10 min. The large-dot film consisted of 9% oxygen following this process, whereas the small-dot films were 6% oxygen.

To evaluate the species formed, we focused on the S 2p XPS peak to analyze the oxidation species, and followed the Pb 4f peak only as a consistency check. Detailed spectral deconvolution of S 2p and Pb 4f high resolution XPS spectra (Supporting Information, Figure

S4 and S5 and Table S2) allowed us to distinguish the sulfur-containing oxidation products polythiol S−S, lead sulfite ($PbSO_3$) and lead sulfate ($PbSO_4$).

For large dots, $PbSO_4$ is present in all samples, whereas $PbSO_4$ appeared in small-dot films only after an extreme accelerated oxidation treatment at 90 °C for 90 min, as shown in Figure 7C, D. For the small dots films, $PbSO_3$ is the principal oxidation product for as-prepared and 10 min annealed samples.

$PbSO_3$ and $PbSO_4$ are known to introduce trap states lying 0.1 and 0.3 eV below the conduction band, respectively.[23,33] For small PbS NCs with bandgap of 1.3 eV, trap states with depth of 0.1 eV introduced by $PbSO_3$ are relatively shallow and act mainly to extend the effective carrier lifetime. However, in large PbS NCs with a bandgap of 0.8 eV, trap states with depth of 0.3 eV introduced by $PbSO_4$ are deep and act mainly as catastrophic recombination centers.

We sought to investigate the different species and rates of oxidation for small-dot *versus* big-dot films. We began from the perspective that, for bulk PbS, the kinetics of oxidation depend on its stoichiometry: sulfur-rich samples oxidize much faster than sulfur deficient samples.[34] Small PbS NCs have a higher Pb to S ratio than large PbS NCs, and thus have less sulfur in the nanocrystal surface. A higher preponderance of Pb^+ on the nanoparticle surface also leads to a denser packing of the ligand shell, providing spatial hindrance to oxygen diffusion.

Finally, we discuss the extent of faceting of small and large dots using XRD and the role of this difference. Large PbS NCs are known to be highly faceted.[35,36] The resultant purely S^- terminated {111} facets[37] are therefore highly vulnerable to oxidation. We present a schematic illustration of this concept in Figure 7E, F. As seen in TEM and XRD (Supporting Information, Figure S1), the small dots are considerably less faceted.

In sum, we have created the first PbS CQD solar cell to exceed 2% AM1.5 PCE. This is also the first infrared solution-processed solar cell to achieve stability in air and under solar illumination. In many respects, the packing, net doping, and recombination in ultraquantum-confined CQD solids are strikingly similar to behavior in their large-dot counterparts. The drastic difference in device stability in air and under solar illumination finds its origins in the significant difference in degree of sulfur-rich surface exposure in small compared to large dots.

Broadly, these findings reinforce the crucial importance not just of size but also of shape in nanomaterials engineered for high performance.

METHODS

Materials. Lead(II) oxide powder (PbO, 99%), oleic acid (OA, technical grade 90%), 1-octadecene (ODE, technical grade 90%), anhydrous toluene, octane, methanol, isoopropyl alcohol, and acetonitrile were purchased from Sigma-Aldrich. Bis(trimethylsilyl) sulfide (TMS, 97% purity) was purchased from Gelest, Inc. 1,2-Ethanedithiol (97%) was purchased from Alpha Aesar.

Synthesis, Isolation, and Treatment of PbS NCs. Synthesis was done with the standard Schlenk line. ODE was degassed by prepumping at 80 °C for 8 h before use. A 0.45 g portion of PbO, 1.5 mL of oleic acid, and 3 mL of ODE was mixed in a two-necked flask and pumped at 95 °C under vacuum for 16 h to produce lead oleate stock solution. We mixed 4.5 mL of lead oleate stock solution and 15 mL of ODE and heated it up to 120 °C using a heating mantle under Ar protection. To this solution, 210 μL of TMS in 10 mL of ODE was swiftly injected, and the solution changed to a brownish color immediately, suggestive of a nucleation burst. The heating mantle was unplugged but was not removed. The solution slowly cooled down to 36 °C in a course of 30−40 min depending on room temperature. Then 20 mL of distilled acetone was injected, and the mixture was stirred for 2 min. PbS NCs were precipitated through centrifugation, redispersed in toluene, and precipitated again through a combination of acetone and centrifugation. Sediments were collected, dried by N_2 gas flow, redispersed in 3 mL of toluene and centrifuged again to precipitate any aggregations and/or reaction side-products. Normally there was very little precipitate at the bottom of the test tube, and 3 mL of PbS NCs were collected for further treatment. Synthesis and isolation processes were all done in air.

Oleylamine Treatment of PbS NCs. On the same day the PbS NCs synthesis took place, 1 mL of prepumped (80 °C for 4 h) oleylamine was added to 3 mL of concentrated PbS NCs toluene solution isolated from synthesis. The mixed solution was stored in a glovebox and was not disturbed for 2 days. Then the dots were precipitated by methanol, isolated, dried, and redispersed in toluene. This entire process is referred to as a cycle. A cycle was repeated three times. Finally, the dots were dispersed in anhydrous octane to produce 10 mg/mL stock solution.

Material Characterization. Visible-near-NIR absorption spectra of PbS NCs in toluene were recorded at room temperature using a Cary 500 UV−vis-near-IR spectrophotometer. Flourier transform infrared spectroscopy (FTIR) spectra were obtained using a Bruker Tensor 27 infrared spectrometer. Samples were prepared on KBr substrates. Powder X-ray diffraction (XRD) was recorded with a Siemens diffractometer with Cu Kα radiation ($\lambda = 1.54178$ Å). PbS NCs were dispersed in isopropyl alcohol and then drop-casted onto Si substrate to produce films with approximately identical thickness. Inductively coupled plasma atomic emission spectroscopy (AES-ICP) measurements were performed using a Perkin-Elmer model Optima 3000DV ICP AEOS. PbS NCs powder was digested completely with nitric acid and diluted with 18 mΩ water to get 100 mL clear solution for AES-ICP measurement. X-ray photoelectron spectroscopy characterization was carried out on PHI 5500 (XPS) spectrometer using Mg Kα source with photon energy of 1253.6 eV. For the study of oxidation, five layer-by-layer film were produced onto ITO substrates in air using 10 mg/mL small and large PbS NCs octane solutions. The LBL process was exactly the same as described in the "device fabrication" section.

Device Fabrication. Chemicals preparation, layer-by-layer spin-coating (LSC), and postannealing were all done in air. Commercial ITO substrates (Delta Technologies, 100 Ω/□, 1 in. by 1 in. squares) were cleaned prior to film deposition in a sequence of 30 min sonification in 1%−3% by volume of Triton X-100 aqueous solution, rinsed with abundant DI water to remove any bubbles, 30 min sonification in isopropyl alcohol, 30 min sonification in deionized water, and finally dried by N_2 flow. Ethanedithiol in acetonitrile (1% by volume) was first prepared. LSC was carried out in a fume hood with good ventilation. The spin-coater was set at 2500 rpm, 15 s duration, and maximized acceleration and deceleration speeds. PbS NCs, 1% EDT solution, anhydrous acetonitrile, and octane used throughout the LSC

process were put into 12 mL plastic syringes capped with 0.2 μm filter.

PbS film was fabricated in air using a layer-by-layer deposition technique. All spin-coating steps were at 2500 rpm. The spin time was set at 15 s, and the acceleration rate was set at maximum. Each iteration in the layer-by-layer deposition consisted of five steps: (1) 5 drops of 10 mg/mL PbS octane solution; (2) 5 drops of 1% (v/v) EDT solution; (3) 10 drops of anhydrous acetonitrile; (4) 10 drops of anhydrous octane; (5) 10 s hair dryer hot air-dry (1.8 kW, ~1 in. from the film). All these five operations were done when the spinning was on. We repeated these steps 15 times to obtain smooth and shinny PbS quantum dot film. The resulting films were 130 ± 10 nm thick as measured by a Dektak profilometer. Films were stored in a desiccator filled with N_2 for 1−4 h and then annealed at 90 °C in air for 5 min before the electrode deposition.

Electrodes were deposited through thermal evaporation in an Edwards 306 evaporator with a pressure of $(1-1.5) \times 10^{-5}$ Torr; 0.8 nm LiF was deposited at a rate of 0.04−0.08 nm/s, followed by 100 nm Al and 100 nm Ag evaporation, both at a rate of 0.5 nm/s. A shadow mask was used to define a 4 × 4 array of 1.92 mm diameter circular contacts.

Device Characterization. *I*−*V* measurements were performed using a Keithley 2400 sourcemeter. *I*−*V* sweeps were performed between −1 and +1 V, with a step size of 0.02 V and a wait time of 100 ms at each point. An Oriel solar simulator operating at 100 mW/cm^2 was used to simulate the solar spectrum under AM1.5G conditions. The output of 632 nm laser diode and the illumination power of solar simulator were calibrated by a Melles−Griot broadband power meter. Capacitance−voltage (*C*−*V*) measurements were performed using an Agilent 4284A precision LCR meter. *C*−*V* sweeps were performed between −0.4 and 0.4 V under Cp−Rp model. The AC signal was set 25 mV and 100 Hz. All measurements were performed in the dark in a shielded and grounded enclosure. For CELIV measurements, an Agilent 33120A function generator was used to generate a linearly increasing voltage pulse with an amplitude of 2 V and a rise time of 20 μs. The carrier extraction profiles were measured across a 50 Ω load with a Tektronix TDS220 digital oscilloscope. For the external quantum efficiency spectrum measurements, the incident light was chopped at 100 Hz and the short circuit current was measured with a Stanford Research SR830 lock-in amplifier. Illumination was provided by a white light source dispersed by a Jobin-Yvon Triax 320 monochromator. Light intensity at different wavelengths was recorded by Newport Optical powermeter (model 1830-C).

Acknowledgment. We thank Vlad Sukhovatkin, Kyle Kemp, Ghada Koleilat, Illan Kramer, and Steven Huang for their assistance and insights. J. Tang thanks Dr. Dan Grozea, Dr. Srebri Petrov and Dr. Haizheng Zhong for material characterization and fruitful discussion. R. Debnath acknowledges the financial support of an e8 scholarship. This publication was supported in part by Award No. KUS-I1-009-21 made by King Abdullah University of Science and Technology (KAUST).

Supporting Information Available: Typical Rietveld refinement of XRD data, summary of XRD analysis, V_{oc} decay, mobility, carrier lifetime and diffusion length calculation, XPS spectra fitting. This material is available free of charge *via* the Internet at http://pubs.acs.org.

REFERENCES AND NOTES

1. Chen, L. M.; Hong, Z.; Li, G.; Yang, Y. Recent Progress in Polymer Solar Cells: Manipulation of Polymer: Fullerene Morphology and the Formation of Efficient Inverted Polymer Solar Cell. *Adv. Mater.* **2009**, *21*, 1434–1449.
2. Sargent, E. H. Infrared Photovoltaics Made by Solution Processing. *Nat. Photon.* **2009**, *3*, 325–331.
3. McDonald, S. A.; Konstantatos, G.; Zhang, S.; Cyr, P. W.; Klem, E. J. D.; Levina, L.; Sargent, E. H. Solution-Processed PbS Quantum Dot Infrared Photodetectors and Photovoltaics. *Nat. Mater.* **2005**, *4*, 138–142.
4. Johnston, K. W.; Pattantyus-Abraham, A. G.; Clifford, J. P.; Myrskog, S. H.; MacNeil, D. D.; Levina, L.; Sargent, E. H. Schottky-Quantum Dot Photovoltaics for Efficient Infrared Power Conversion. *Appl. Phys. Lett.* **2008**, *92*, 151115.
5. Luther, J. M.; Law, M.; Beard, M. C.; Song, Q.; Reese, M. O.; Ellingson, R. J.; Nozik, A. J. Schottky Solar Cells Based on Colloidal Nanocrystal Films. *Nano Lett.* **2008**, *8*, 3488–3492.
6. Ma, W.; Luther, J. M.; Zheng, H.; Wu, Y.; Alivisatos, A. P. Photovoltaic Devices Employing Ternary PbS_xSe_{1-x} Nanocrystals. *Nano Lett.* **2009**, *9*, 1699–1703.
7. Schaller, R. D.; Klimov, V. I. High Efficiency Carrier Multiplication in PbSe Nanocrystals: Implications for Solar Enger Conversion. *Rhys. Rev. Lett.* **2004**, *92*, 186601.
8. Luther, J. M.; Beard, M. C.; Song, Q.; Law, M.; Ellignson, R. J.; Nozik, A. J. Multiple Exciton Generation in Films of Electronically Coupled PbSe Quantum Dots. *Nano Lett.* **2007**, *7*, 1779–1784.
9. Sukhovatkin, V.; Hinds, S.; Brzozowski, L.; Sargent, E. H. Colloidal Quantum-Dot Photodetectors Exploiting Multiexciton Generation. *Science* **2009**, *324*, 1542–1544.
10. Hines, M. A.; Scholes, G. D. Colloidal PbS Nanocrystals with Size-Tunable Near-Infrared Emission: Observation and Postsynthesis Self-Narrowing of the Particle Size Distribution. *Adv. Mater.* **2003**, *15*, 1844–1849.
11. Murphy, J. E.; Beard, M. C.; Norman, A. G.; Ahrenkiel, S. P.; Johnson, J. C.; Yu, P. R.; Micic, O. I.; Ellingson, R. J.; Nozik, A. J. PbTe Colloidal Nanocrystals: Synthesis, Chracterization, and Multiple Exciton Generation. *J. Am. Chem. Soc.* **2006**, *128*, 3241–3247.
12. Moreels, I.; Lambert, K.; Smeets, D.; Muynck, D. D.; Nollet, T.; Martins, J. C.; Vanhaecke, F.; Vantomme, A.; Delerue, C.; Allan, G.; Hens, Z. Size-Dependent Optical Properties of Colloidal PbS Quantum Dots. *ACS Nano,* **2009**, *3*, 3023–3030.
13. Kang, I.; Wise, F. W. Electronic Structure and Optical Properties of PbS and PbSe Quantum Dots. *J. Opt. Soc. Am. B* **1997**, *14*, 1632–1646.
14. *Topas, v. 2.1, General Profile and Structure Analysis Software for Powder Diffraction Data*, *User's Manual*; Bruker AXS: Karlsruhe, Germany, 2003.
15. Smith, A. M.; Mohs, A. M.; Nie, S. Tuning the Optical and Electronic Properties of Colloidal Nanocrystals by Lattice Strain. *Nat. Nanotechnol.* **2009**, *4*, 56–63.
16. Dai, Q.; Wang, Y.; Li, X.; Zhang, Y.; Pellegrino, D. J.; Zhao, M.; Zou, B.; Seo, J.; Wang, Y. D.; Yu, W. W. Size-Dependent Composition and Molar Extinction Coefficient of PbSe Semiconductor Nanocrystals. *ACS Nano* **2009**, *3*, 1518–1524.
17. Moreels, L.; Fritzinger, B.; Martins, J. C.; Hens, Z. Surface Chemistry of Collodial PbSe Nanocrystals. *J. Am. Chem. Soc.* **2008**, *130*, 15081–15086.
18. Talapin, D. V.; Murray, C. B. PbSe Nanocrystal Solids for n- and p-Channel Thin Film Field-Effect Transistors. *Science* **2005**, *310*, 86–89.
19. Klem, E. J. D.; MacNeil, D. D.; Cyr, P. W.; Levina, L.; Sargent, E. H. Efficient Solution-Processed Infrared Photovoltaic Cells: Planarized All-Inorganic Bulk Heterojunction Devices *via* Inter-Quantum-Dot Bridging during Growth from Solution. *Appl. Phys. Lett.* **2007**, *90*, 183113.
20. Koleilat, G.; Levina, L.; Shukla, H.; Myrskog, S. H.; Hinds, S.; Pattantyus-Abraham, A. G.; Sargent, E. H. Efficient, Stable Infrared Photovoltaics Based on Solution-Cast Colloidal Quantum Dots. *ACS Nano* **2008**, *2*, 833–840.
21. Luther, J. M.; Law, M.; Song, Q.; Perkins, C. L.; Beard, M. C.; Nozik, A. J. Structural, Optical, and Electrical Properties of Self-Assembled Films of PbSe Nanocrystals Treated with 1,2-Ethanedithiol. *ACS Nano* **2008**, *2*, 271–280.
22. Barkhouse, D. A. R.; Pattantyus-Abraham, A. G.; Levina, L.; Sargent, E. H. Thiols Passivate Recombination Centers in Colloidal Quantum Dots Leading to Enhanced Photovoltaic Device Efficiency. *ACS Nano* **2008**, *9*, 40–44.
23. Konstantatos, G.; Levina, L.; Fisher, A.; Sargent, E. H. Engineering the Temporal Response of Photoconductive Photodetectors *via* Selective Introduction of Surface Trap States. *Nano Lett.* **2008**, *8*, 1446–1450.

24. Li, Y. S.; Li, S. FTIR Spectra of $HSCH_2CH_2SH$, CH_3SCH_2SH, and CH_3SSCH_3 in Argon and Nitrogen Matrices. *Spectrochimica Acta A* **1994**, *50*, 509–519.
25. Sun, B.; Findikoglu, A. T.; Sykora, M.; Werder, D. J.; Klimov, V. I. Hybrid Photovoltaics Based on Semiconductor Nanocrystals and Amorphous Silicon. *Nano Lett.* **2009**, *9*, 1235–1241.
26. Tang, J.; Wang, X. W.; Brzozowski, L.; Barkhouse, D. A. R. ; Debnath, R.; Levina, L.; Sargent, E. H. Schottky Quantum Dot Solar Cells Stable in Air under Solar Illumination. *Adv. Mater.*, published online January 7, 2010, http://dx.doi.org/10.1002/adma.200903240.
27. Hyun, B.-R.; Zhong, Y.-W.; Bartnik, A. C.; Sun, L.; Abrunna, H. D.; Wise, F. W.; Goodreau, J. D.; Matthews, J. R.; Leslie, T. M.; Borrelli, N. F. Electron Injection from Colloidal PbS Quantum Dots into Titanium Dioxide Nanoparticles. *ACS Nano* **2008**, *2*, 2206–2212.
28. Juska, G.; Viliunas, M.; Arlauskas, K.; Nekrasas, N. Hole Drift Mobily in μc-Si:H. *J. Appl. Phys.* **2001**, *89*, 4971–4974.
29. Johnston, K. W.; Pattantyus-Abraham, A. G.; Clifford, J. P.; Myrskog, S. H.; Hoogland, S.; Shukla, H.; Klem, E. J. D.; Levina, L.; Sargent, E. H. Efficient Schottky-Quantum Dot Photovoltaics: The Roles of Depletion, Drift, and Diffusion. *Appl. Phys. Lett.* **2008**, *92*, 122111.
30. Malliaras, G. G.; Salem, J. R.; Brock, P. J. Photovoltaic Measurement of the Built-in Potential in Organic Light Emitting Diodes and Photodiodes. *J. Appl. Phys.* **1998**, *84*, 1583–1587.
31. Clifford, J. P.; Konstantatos, G.; Johnston, K. W.; Hoogland, S.; Levina, L.; Sargent, E. H. Fast, Sensitive and Spectrally Tuneable Colloidal-Quantum-Dot Photodetectors. *Nat. Nanotechnol.* **2008**, *9*, 40–44.
32. NIST XPS database, http://srdata.nist.gov/xps/, accessed on Sept. 15, 2009.
33. Konstantatos, G.; Sargent, E. H. PbS Colloidal Quantum Dot Photoconductive Photodetectors: Transport, Traps and Gain. *Appl. Phys. Lett.* **2007**, *91*, 173505.
34. Eadington, P.; Prosser, A. P. Oxidation of Lead Sulfide in Aqueous Suspensions. *Trans. Inst. Min. Metall.* **1969**, *78*, 74–82.
35. Fan, D. B.; Thomas, P. J.; O'Brien, P. Pyramidal Lead Sulfide Crystallites with High Energy {113} Facets. *J. Am. Chem. Soc.* **2008**, *130*, 10892–10894.
36. Warner, J. H.; Cao, H. Shape Control of PbS Nanocrystals Using Multiple Surfactants. *Nanotechnology* **2008**, *19*, 305605.
37. Cho, K. S.; Talapin, D. V.; Gaschler, W.; Murray, C. B. Designing PbSe Nanowires and Nanorings through Oriented Attachment of Nanoparticles. *J. Am. Chem. Soc.* **2005**, *127*, 7140–7147.